

Influx of nitrogen-rich material from the outer Solar System indicated by iron nitride in Ryugu samples

Received: 17 December 2022

Accepted: 19 October 2023

Published online: 30 November 2023

 Check for updates

A list of authors and their affiliations appears at the end of the paper

Large amounts of nitrogen compounds, such as ammonium salts, may be stored in icy bodies and comets, but the transport of these nitrogen-bearing solids into the near-Earth region is not well understood. Here, we report the discovery of iron nitride on magnetite grains from the surface of the near-Earth C-type carbonaceous asteroid Ryugu, suggesting inorganic nitrogen fixation. Micrometeoroid impacts and solar wind irradiation may have caused the selective loss of volatile species from major iron-bearing minerals to form the metallic iron. Iron nitride is a product of nitridation of the iron metal by impacts of micrometeoroids that have higher nitrogen contents than the CI chondrites. The impactors are probably primitive materials with origins in the nitrogen-rich reservoirs in the outer Solar System. Our observation implies that the amount of nitrogen available for planetary formation and prebiotic reactions in the inner Solar System is greater than previously recognized.

The nitrogen distribution in primitive materials is an indicator of the chemical evolution in the early Solar System¹. Recent remote-sensing studies have suggested that comets and icy bodies in the outer Solar System have large inventories of solid nitrogen compounds, such as ammonium salts^{2,3}. Although some ammonium components can be stable in the near-Earth region², they have not been identified in interplanetary dust particles and Antarctic micrometeorites that may have been delivered to Earth from these bodies. Therefore, the compositional link between the cosmic dust transported to the near-Earth region and the small icy bodies remains elusive. Isotope analyses of lunar ilmenite grains have revealed that the supply of exogenous nitrogen to the lunar surface is from asteroidal micrometeoroids infalling to the Moon⁴, but the nitrogen abundance in the micrometeoroids has not been quantified.

The Japan Aerospace Exploration Agency (JAXA)'s Hayabusa2 spacecraft has explored the near-Earth C-type asteroid Ryugu and brought back surface material^{5,6}. The Ryugu samples are chemically primitive and consistent with CI carbonaceous chondrites^{7–9}. Ryugu grains have experienced cumulative surface modifications, known as space weathering, which are caused by micrometeoroid impacts and solar wind implantation¹⁰. Evidence of space weathering in Ryugu

samples may provide unique clues to the supply of primitive material to the orbit of Ryugu and its properties by comparison with the chemical composition of Ryugu.

Exogenous nitrogen could become trapped in lunar regolith by chemisorption or by the formation of nitride with silicon or titanium⁴, but no mineralogical observation has been reported for the formation of nitrogen-bearing compounds on airless surfaces. Studies of regolith samples from the Moon and the S-type asteroid Itokawa suggest that metallic iron is the representative product of space weathering of silicate minerals and iron sulfides^{11–13}. Due to the high reactivity of iron metal, these could react with exogenous components when they are formed at space-exposed surfaces. In Ryugu grains, space-weathered phyllosilicates show that there has been a reduction of Fe³⁺ to Fe²⁺, whereas metallic iron particles rarely appear in impact-melted phyllosilicates¹⁰. Therefore, the origin of metallic iron in the highly oxidized environment of Ryugu and its interaction with exogenous materials remain open questions. In this study, we investigated iron sulfides, magnetite and carbonate, which are the major iron-bearing minerals in Ryugu samples^{7,8,14}, but the chemical state of iron due to space weathering has not been analysed.

✉ e-mail: matsumoto.toru.2z@kyoto-u.ac.jp

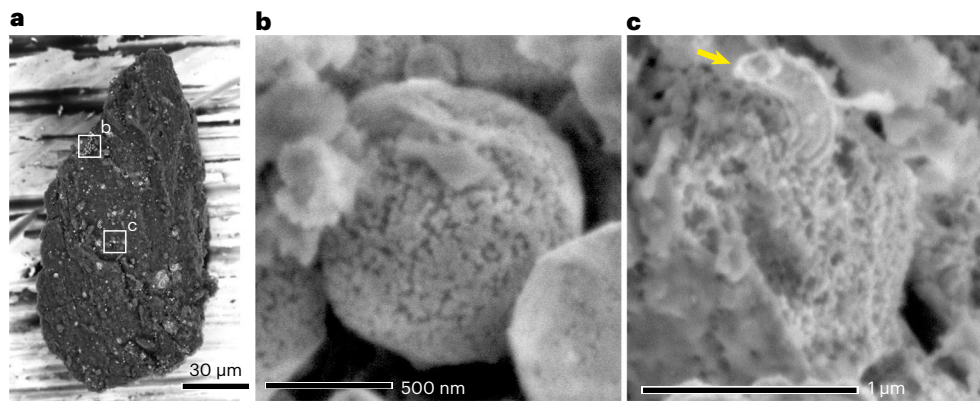


Fig. 1 | Modified magnetite and iron sulfides on a Ryugu grain. **a**, Backscattered electron image of a fine Ryugu grain. The white boxes correspond to the areas shown in **b** and **c**. **b**, Secondary electron image of framboidal magnetite showing

granular texture. **c**, Secondary electron image of porous iron sulfide surrounded by phyllosilicate. The arrow points to an iron whisker on the iron sulfide surface. Sample ID is A0104-021012.

Results

Space-exposed surfaces of Ryugu grains, including magnetite, iron sulfides and carbonate, were examined using scanning electron microscopy (SEM), scanning transmission electron microscopy (STEM) and transmission electron microscopy (TEM) (Methods). We identified Ryugu grains showing surface modifications related to space weathering with SEM (Fig. 1 and Supplementary Table 1). The modified surfaces of framboidal, spherulitic and plaquette magnetite grains have granular surfaces (Fig. 1b and Supplementary Fig. 1). The modified surfaces of iron sulfides have abundant <100-nm-sized depressions and pores, when they coexist with the modified magnetite (Fig. 1c and Supplementary Figs. 1 and 2). Elongated and curved iron metal often protrude from the sulfide surfaces.

The surface modification of three magnetite grains (two framboids, A0104-021012 and A0104-028098, and one spherulite, A0104-026006) was investigated by STEM. The magnetite surfaces are covered by granular iron-rich layers (Fig. 2, Extended Data Fig. 1 and Supplementary Fig. 3). The Fe/O ratio in the magnetite increases towards the uppermost iron-rich layers. The iron-rich layers are enriched in silicon and magnesium. In addition, those in A0104-026006 and A0104-028098 are also rich in sulfur (up to ~5 at.%) and nitrogen (up to ~9 at.%) (Fig. 2 and Extended Data Fig. 1). Crystallographic distortion appears in the magnetite beneath the iron-rich layers (Extended Data Fig. 1). Nanobeam electron-diffraction patterns from the iron-rich layer in A0104-026006 indicate the appearance of body-centred cubic (bcc) iron metal and a cubic crystal having the lattice parameters of roaldite (Fe_4N)¹⁵ (Extended Data Fig. 1). The positions of the $\text{Fe}_{L_{2,3}}$ edges of the electron energy-loss spectra obtained from the iron-rich layer shift to lower energy-losses compared to magnetite, suggesting that the iron is in lower oxidation states in the iron-rich layer¹⁶ (Fig. 3). The iron-rich layer in A0104-028098 is dominated by a cubic crystal having a lattice constant approximately 2% larger than the typical value of roaldite (0.379 nm; ref. 15) (Fig. 2). When the diffraction patterns of the cubic crystal are assigned to roaldite, their 200 diffraction spots are close to the 400 spots from magnetite. These spots come from the atomic arrangement of iron in roaldite and the iron in tetrahedral sites in magnetite, respectively¹⁷ (Extended Data Fig. 2). The crystallographic relationship between the two minerals has been reported in synthetic Fe_4N (ref. 18) and is probably due to the similar arrangements of these particular iron atoms. The cubic crystal does not have diffraction spots that correspond to superlattice structures of nitrogen ordering in roaldite, probably due to damage by the electron beam during the TEM observations¹⁸. These crystallographic features have also been observed in Fe_4N crystals epitaxially grown on oxide substrates¹⁹. Therefore, the cubic crystal in A0104-028098 may also be

Fe_4N . The iron-rich layer in A0104-021012 includes bcc iron metal but does not show enrichment of nitrogen or sulfur (Supplementary Fig. 4).

The iron whiskers on iron sulfides consist both of bcc iron and face-centred-cubic (fcc) iron with <51 at.% of Ni (Extended Data Fig. 3). The modified iron sulfides we observed are composed of 4C pyrrhotite (Fe_7S_8), NC pyrrhotite (Fe_{1-x}S), troilite (FeS) and pentlandite (Supplementary Table 2). Troilite appears predominantly in the modified iron sulfides (Extended Data Fig. 3) or occurs as the major phase within the modified areas of sulfides (Extended Data Fig. 4). Nanobeam electron-diffraction patterns within a depth of <10 nm from the sulfide surface are composed only of diffraction spots from the basic hexagonal NiAs-type structure (the 1C subcell) (Extended Data Figs. 3 and 4). This indicates the disappearance of atomic ordering at the surface over distances longer than the 1C subcell. The iron sulfides and iron metal are covered by thin layers (30–40 nm thick) rich in silicon and magnesium (Extended Data Fig. 4).

Brunnerite ($(\text{Mg},\text{Fe})\text{CO}_3$) is covered by a layer of ferroperricite with a cation ratio of $\text{Mg}/(\text{Mg} + \text{Fe} + \text{Mn}) = -0.75$ (Extended Data Fig. 5), although no iron metal exists at the surface. Crystallographic distortions appear in the substrate brunnerite within 110–130 nm below the surface. Carbon and oxygen are depleted at the surface of the brunnerite, whereas silicon and sulfur were detected at the uppermost surfaces of the modified carbonate (Supplementary Fig. 5).

These surface-modified magnetite grains and sulfides usually coexist with phyllosilicates having smooth or frothy surfaces (Supplementary Table 1 and Supplementary Fig. 1). Approximately 100-nm-thick amorphous rims have developed on the smooth phyllosilicates (Extended Data Fig. 6). These structures are observed in space-weathered phyllosilicates¹⁰. Submicrometre-sized craters and melt deposits appear on some of the phyllosilicate and carbonate surfaces (Extended Data Fig. 7). A small crater on the smooth phyllosilicate surface consists of an amorphous crater floor that is rich in Ca and Fe (Supplementary Fig. 6) and has vesicles showing a sharp π^* pre-edge peak at 531 eV in the oxygen K-edge of electron energy-loss spectra (Extended Data Fig. 7), indicating molecular oxygen-bearing species²⁰.

Discussion

Identification of space-weathered structures of iron-bearing minerals

The space-weathered structures of magnetite and carbonate have not been investigated so far, whereas the modified microstructures of iron sulfides, including iron whiskers and the disappearance of superstructures, are the main features of space-weathered iron sulfides found on the Moon and Itokawa^{21,22}. The coexistence of modified magnetite and carbonate with space-weathered sulfides and phyllosilicates

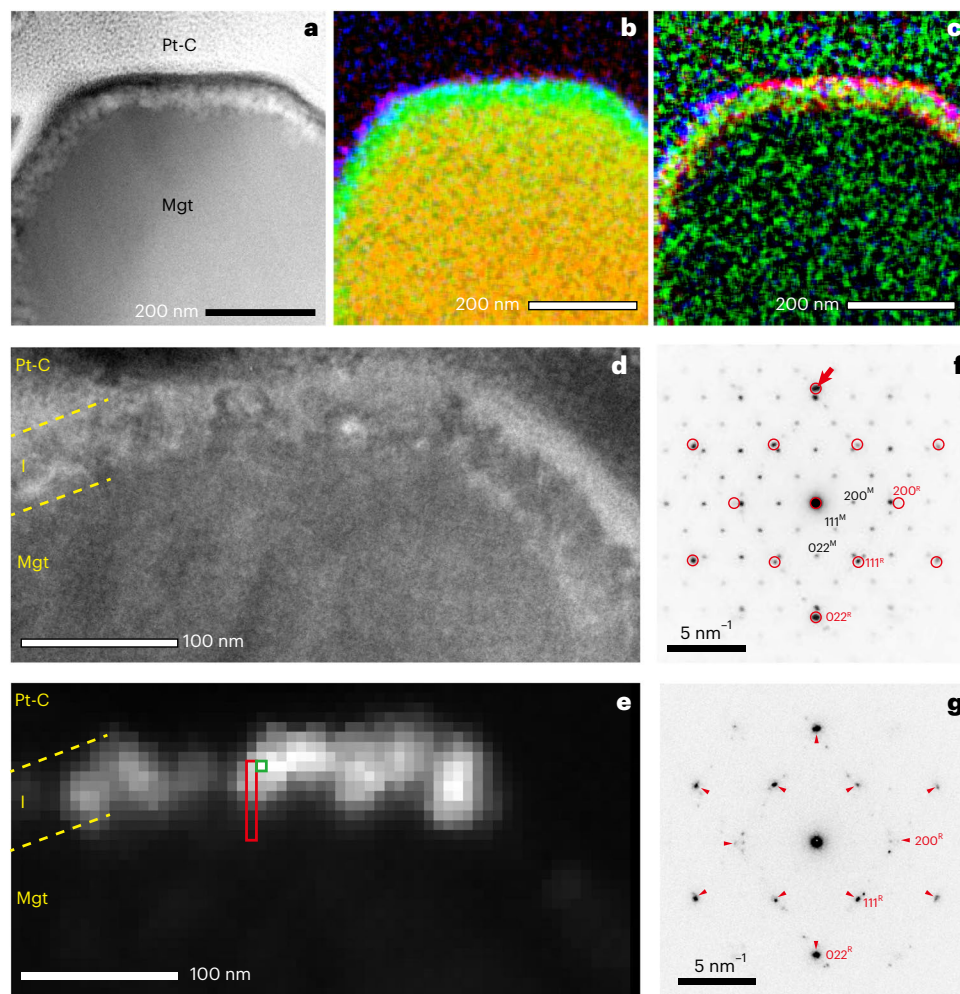


Fig. 2 | TEM and STEM analysis of modified framboidal magnetite in a Ryugu grain. **a**, HAADF-STEM image of modified magnetite (Mgt). Pt-C is the protective platinum coat. **b,c**, STEM-EDX elemental maps of the modified magnetite. An RGB composite image of oxygen (red), iron (green) and silicon (blue) is shown in **b** and that of sulfur (red), nitrogen (green) and magnesium (blue) is in **c**. **d,e**, BF-TEM image (**d**) and DF-STEM image (**e**) of modified magnetite constructed from a STEM-NBD dataset. The DF-STEM image in **e** was produced by selecting a diffraction spot of roaldite, indicated in **f**. Dashed lines denote the boundaries of the iron-rich layer (l). The white areas in **e** correspond to high-intensity regions

for the diffraction spot of roaldite. **f**, Position-averaged NBD pattern for the rectangular region covering the iron-rich layer and the substrate magnetite in **e**. Red circles indicate diffraction spots from roaldite (superscript R), which has a crystallographic relationship with magnetite (superscript M). The arrow shows the diffraction spot of roaldite chosen for producing the DF-STEM image in **e**. **g**, NBD pattern from the iron-rich layer in **e**. Diffraction spots of roaldite (arrowed) are dominant, and those of magnetite are weak in the layer. Sample ID is A0104-028098.

indicates that their surface modifications could have been derived from similar events. Further evidence for the space exposure of these minerals is their coexistence with melted deposits and micrometre-sized craters, which may have experienced impact-induced compaction and vaporization to form the amorphous materials and the gas-filled vesicles in phyllosilicates. The areas with crystallographic damage (Extended Data Figs. 1 and 5) are typical structures formed by the solar wind¹³. In addition, the depths of these structures are roughly consistent with the penetration depth of the solar wind²³ (H^+ and He^+ with typical energies of 1 keV per nucleon) (Supplementary Fig. 7). The outermost silicon- and magnesium-rich layers on the iron-bearing minerals are chemically distinct from the substrates and probably correspond to vapour-deposited materials generated by solar wind sputtering and micrometeoroid bombardment on nearby regolith grains^{11,13}.

Formation of metallic iron and selective escape of volatiles

The occurrence of metallic iron on magnetite and iron sulfides on the oxidized surface of Ryugu indicates that the decomposition of iron-bearing minerals by space weathering is not affected by the bulk

oxidation state of small bodies. Previous studies of Itokawa and lunar grains proposed that the iron whiskers on sulfides grew through the production of excess iron atoms caused by selective sulfur escape from the sulfide surface as a result of solar wind implantation, micrometeoroid bombardment or thermal cycling^{21,22}. Taenite in iron whiskers has been found only in Ryugu samples, to date, probably because of the higher amount of Ni in the sulfides. The common appearance of troilite (FeS) in the modified sulfides suggests that non-stoichiometric pyrrhotites ($Fe_{1-x}S$) have been converted to troilite due to sulfur loss preceded by space weathering.

Like the effects of space weathering effects on sulfides, the iron metal in magnetite and the high Fe/O ratio near its surface may have been formed by the selective escape of oxygen due to ion sputtering and thermal effects of micro-impacts that promote atomic diffusion. We identified an increase of the Fe/O ratio for magnetite in Ryugu grains after helium ion irradiation (Extended Data Fig. 8), consistent with a previous study²⁴. The oxygen atoms may leave in the form of radicals or oxygen molecules, causing the decomposition of magnetite. In addition, the chemical reaction of magnetite with accumulated solar

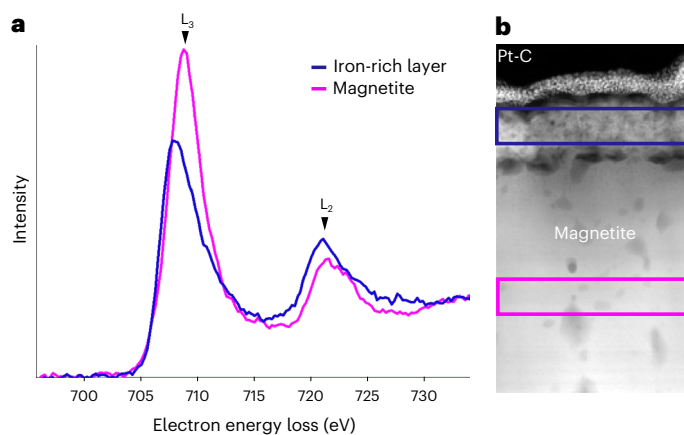


Fig. 3 | Fe L_2 and L_3 EELS spectra of magnetite and iron-rich layer in a Ryugu grain. a, Fe L_2 and L_3 EELS spectra obtained from the iron-rich layer (blue) and magnetite (magenta) as a function of electron energy loss (eV, electron volt) (x axis) and normalized intensity (arbitrary unit) (y axis). Arrowheads indicate peaks of the Fe L_2 and L_3 edges. Magnetite has a Fe L_3 peak position at 709.03 eV whereas the iron-rich layer has a Fe L_3 peak position at 708.03 eV. **b**, HAADF-STEM image (164 nm \times 298 nm) showing the selected regions for EELS spectra (blue, iron-rich layer and magenta, magnetite). Pt-C is the platinum coat. Sample ID is A0104-026006.

wind hydrogen could cause oxygen loss through the following reaction: $\text{Fe}^{2+}\text{Fe}_2^{3+}\text{O}_4 + 4\text{H}_2 \rightarrow 3\text{Fe}^0 + 4\text{H}_2\text{O}$. Notably, the morphologies of iron metal grains are different between magnetite and iron sulfides. The self-diffusion coefficient of iron in magnetite²⁵ is several orders of magnitudes lower than in iron sulfides²⁶ through a wide range of temperatures and oxygen fugacities. Iron nanoparticles on magnetite may have nucleated from excess iron atoms in the vicinity, whereas iron whiskers may be derived from excess iron atoms that diffused long distances to the limited nucleation sites on iron sulfides, perhaps through accelerated surface or grain boundary diffusion. Each iron nanoparticle in magnetite has a much larger surface-to-volume ratio than iron whiskers and is expected to be highly chemically reactive.

The surface of carbonate may also have experienced the selective escape of carbon and oxygen without being fully reduced to metallic iron, in contrast to our observations of iron sulfides and magnetite. The escape of the volatiles is probably resulted in the formation of the ferropiclasite rim on breunnerite. Alternatively, solar wind hydrogen could have reacted with breunnerite to form methane or produce reducing conditions that cause carbonate decarboxylation²⁷.

Nitridation of the space-weathered surfaces

The concentration of nitrogen at the surface of the magnetite is in stark contrast to other moderately to highly volatile elements, including H, C, O and S, which are released from the space-weathered iron-bearing minerals and phyllosilicates¹⁰. There may be effective mechanisms for fixing nitrogen or nitrogen-rich sources. Roaldite has been identified in iron meteorites as the exsolved phase in kamacite¹⁵ and in carbonaceous chondrites as the products of NH_3 -rich nebular gas²⁸, whereas the formation of nitride on airless surfaces has not been reported. The iron nitride we observed is probably the first mineralogical evidence of nitrogen fixation associated with space weathering. The appearance of iron metal on magnetite with and without nitrogen indicates that metal growth occurred before nitrogen incorporation. This suggests that the iron nitride on magnetite may have formed through nitridation of the iron metal. We exclude the possibility that the nitride was formed by terrestrial nitrogen gases during sample storage, because although all the Ryugu grains we analysed were exposed to ambient gases during storage, a nitrogen concentration was observed in only two out of the three space-weathered Ryugu grains, not in all grains.

Iron nitride (Fe_4N) with a thickness of 50 nm (Fig. 2) contains nitrogen atoms at a density of 9.2×10^{16} atoms cm^{-2} (Methods). The supply rate of nitrogen atoms to the magnetite surface has been calculated as $4\text{--}6 \times 10^5$ atoms $\text{cm}^{-2} \text{s}^{-1}$, considering that the density of the solar flare tracks in olivine¹⁰, which coexists with the space-weathered iron sulfides and magnetite, corresponds to a residence time of $5\text{--}7 \times 10^3$ yr in the upper few millimetres of Ryugu's regolith surface. This rate is 20–300 times higher than the supply rate of exogenous nitrogen estimated in lunar ilmenite ($0.2\text{--}2 \times 10^4$ atoms $\text{cm}^{-2} \text{s}^{-1}$)⁴. The solar wind is one possible source of nitrogen concentration. An exposure age of 10^5 yr at 1.19 AU (the current average heliocentric distance of Ryugu) has been calculated based on the accumulation of solar wind nitrogen to produce 50-nm-thick iron nitride, assuming an ideal case in which solar nitrogen is directly implanted in the magnetite surface and all nitrogen atoms are consumed to form iron nitride (Methods). This exposure age is far longer than the solar flare track ages and the longest solar wind exposure ages of 3,500 yr for Ryugu samples²⁹. Therefore, nitrogen in the solar wind may not be a major contributor to the nitridation. The solar wind could also have caused the sputtering of nitrogen atoms in insoluble organic matter (IOM), the primary nitrogen-bearing phase in Ryugu. Subsequently, nitrogen atoms could have been implanted into magnetite surfaces. Considering the high nitrogen-to-carbon atomic ratio of 0.01–0.035 in the IOM³⁰, iron carbide could have been formed by the carbon sputtered from the IOM. The dominance of iron nitrides suggests that sputtering is not a major cause of nitridation.

Another possible origin for nitridation is nitrogen compounds in vapour produced by micrometeoroid impacts. Micrometeoroids composed of carbonaceous chondritic materials are rich in nitrogen in organic form. CI chondrites have the highest nitrogen content among carbonaceous chondrites³¹. We, therefore, hypothesized impacts of CI chondritic micrometeoroids that produced CI chondritic vapour by impact-induced vaporization of the micrometeoroids or Ryugu's materials. Molecular N_2 and NH_3 are nitriding agents for iron metal and are major nitrogen compounds in equilibrated vapour with a CI chondritic composition^{32,33}. Ammonia gas can be readily dissociated with metal catalysis, causing absorption and diffusion of nitrogen atoms in the metal³⁴. When iron metal is exposed to NH_3 gas in impact vapour, nitridation by water-rich CI gas competes with oxidation. According to the Fe–O–N potential diagram, equilibrated CI vapour is expected to stabilize magnetite rather than iron nitride due to high oxygen fugacity (Extended Data Fig. 9 and Methods). Molecular N_2 is more abundant than ammonia gas in the modelled vapour but is poorly dissociated for nitridation due to the strong triple bond. If all the N_2 in the modelled vapour is converted to ammonia by the Haber–Bosch process ($\text{N}_2 + 3\text{H}_2 = 2\text{NH}_3$) with the bcc iron catalyst³⁵, the maximum $\log([\text{NH}_3]/[\text{H}_2]^{3/2})$ ($\text{bar}^{-1/2}$) value of -1.4 is obtained at 500 K. The gas compositions are not plotted in the stability field of Fe_4N in the potential diagram in Extended Data Fig. 9. Accordingly, nitridation of Ryugu iron may require more reducing conditions or vapour with ammonia-rich compositions.

The necessary reducing conditions may have been achieved locally on the surface of magnetite by the accumulation of solar wind hydrogen. Otherwise, when impact vapour is produced from space-weathered surfaces in which the dehydration of phyllosilicate proceeds, the vapour could be depleted in H_2O and have low oxygen fugacity. However, high carbon contents compared to nitrogen in Ryugu³⁰ would probably cause the formation of iron carbide rather than nitride in the reduced conditions. Experimental studies have shown that carbon-rich gas mixtures of $\text{NH}_3\text{--H}_2\text{--CO--CO}_2\text{--H}_2\text{O}$ produce iron carbides faster than nitride³⁶. This is due to the lower solubility of carbon in iron compared to nitrogen. Therefore, the iron nitride could have been produced by vapour from Ryugu's materials that is richer in nitrogen than carbon. It has been suggested that NH-rich compounds and NH-bearing organics occur within the interlayers of phyllosilicates in Ryugu samples^{37,38}, but a large clump of nitrogen-dominated

materials has not been found in Ryugu samples^{30,39}. Nitrogen-rich reservoirs on Ryugu could possibly occur in extremely nitrogen-rich lithology that has not yet been observed by laboratory analysis or in ammonia-bearing ices preserved in the permanently shadowed regions where volatile species are trapped in the localized cold environment.

Alternatively, we suggest that nitridation may have occurred through impacts of exogenous source(s) containing NH_3 compounds. The exotic source should contain NH_3 precursors in refractory solids. NH_3 -rich ices can be excluded as they would have sublimated on their journey to Ryugu. Nitrogen-rich IOM has been found in dust samples from the comet Wild2 (ref. 40), chondritic porous interplanetary dust particles (IDPs)^{40,41} and ultracarbonaceous Antarctic micrometeorites⁴², which are thought to be delivered to Earth from comets or small icy bodies. Ammonia-rich IOM in CR chondrites indicates that ammonia is pervasive in the parent body⁴³. Carbon is predominant in such IOM, although the lack of evidence of carbonization on the magnetite grain surfaces may require the presence of other nitrogen-rich exogenous materials.

NH_4^+ salts have been detected as major components of the surface materials on the dwarf planet Ceres³ and on comets². These salts are probably widely distributed beyond the main asteroid belt³. Given a large influx of cometary dust towards the inner solar region⁴⁴, nitridation on the magnetite surface could have been caused by micro-impacts of nitrogen-rich dust falling onto Ryugu. Due to their relative high velocity⁴⁵, the impactors would have fully evaporated and locally produced ammonia-rich vapour. Such dust particles could be rich in sulfur. For example, the organic materials in ultracarbonaceous Antarctic micrometeorites contain a considerable amount of sulfur⁴², and possible anion species of ammonium salts in comets include sulfate². This may explain the strong correlation between the presence of nitrogen and sulfur, although sulphurization of iron metal can also occur in vapour with a Cl composition (Extended Data Fig. 9). The magnetite surface could have experienced nitridation more than once, because space exposure may have occurred several times due to grain motion during regolith gardening, as suggested by the distribution of the space-weathered sulfides on different grain surfaces (Supplementary Fig. 2).

In this study, we propose that iron nitride on magnetite surfaces may have been formed by impacts of nitrogen-rich dust, but the contribution from Ryugu's materials cannot be excluded. Future analysis of the $^{14}\text{N}/^{15}\text{N}$ ratio will further constrain the origin of the nitride, because the isotopic ratio varies across the Solar System¹. If nitrogen-rich dust is present in the orbit of Ryugu, dust impacts may have occurred in the near-Earth region, because the regolith residence time of surface and subsurface materials on Ryugu (~5 Myr) is consistent with the resurfacing timescale after Ryugu migrated from the main asteroid belt into its current near-Earth orbit²⁹. However, most chondritic porous IDPs and micrometeorites have bulk nitrogen-to-carbon ratios like those of carbonaceous chondrites⁴⁶. It has been proposed that nitrogen-bearing salts are probably contained in cometary IDPs but are lost during atmospheric entry². The nitridation on Ryugu may correspond to evidence of nitrogen transport in refractory solid form, such as salts, towards Ryugu's current orbit, and implies that dust reaching the inner Solar System has nitrogen contents higher than would be expected from bulk contents in most IDPs and Antarctic micrometeorites. Nitrogen components avoiding sublimation could have been available during the accretion of Earth⁴⁷ and for prebiotic reactions on Earth⁴⁸.

Methods

Sample preparation

Ryugu samples from the first and second touchdown sites were preserved in chambers A and C of the sample catcher inside the sample container of the Hayabusa2 spacecraft, respectively. Fine grains (average grain size is ~100 μm across) were taken from both chambers at the Extraterrestrial Sample Curation Center of JAXA. After the samples were allocated by JAXA, they were handled in a dry glovebox filled

with nitrogen at Kyoto University. For the surface observations, the fine grains were fixed on gold plates using an epoxy adhesive. At Kyoto University, coarse Ryugu grains (millimetre-sized grains) from the first touchdown site (A0026) were fixed with Araldite epoxy onto an aluminium stage. Coarse grains (A0067 and A0094) were fixed on indium plates at Tohoku University. Fragments of a coarse grain from the second touchdown site (C0002) were fixed onto a gold plate at Kyoto University. The space-weathered features on phyllosilicates of these samples were described in a previous study¹⁰.

SEM analysis

Surface features of >500 grains from chamber A (average diameter ~71 μm) and >300 fine grains from chamber C (average diameter ~57 μm) from the sample canister were observed using a field emission SEM (FE-SEM; JEOL JSM-7001F) and a focused ion beam SEM (FIB-SEM; Helios NanoLab G3 CX, Thermo Fisher Scientific) at Kyoto University and by FIB-SEM (Scios, Thermo Fisher Scientific) at Kyushu University. To avoid damage by the electron beam, the samples were observed at 2 kV acceleration voltage with an electron beam current of ~15–80 pA at Kyoto University, and 3 kV acceleration voltage with an electron beam current of 25 pA at Kyushu University. Elemental mapping analyses were performed with an energy-dispersive X-ray spectrometer (EDX) using the FE-SEM (JSM-7001F) equipped with an X-Max^N 150 mm² (Oxford Instruments) at Kyoto University. An electron beam with a 15 kV acceleration voltage and an electron beam current of ~100 pA was applied for the EDX analysis. The surface features of a coarse grain (A0026) were observed using FE-SEM (Hitachi SU6600) at the Institute of Space and Astronautical Science within JAXA. The surface features of coarse grains (A0067, A0094 and C002) were observed using FIB-SEM (Helios NanoLab G3 CX, Thermo Fisher Scientific) at Kyoto University.

TEM analysis

Electron-transparent sections of regions of interest on the fine Ryugu grains were extracted for TEM and STEM studies using a FIB system (Helios NanoLab G3 CX) at Kyoto University. To protect the grain surfaces during FIB processing and enhance the electrical conductivity, Ryugu grains were coated with an electron-beam-deposited Pt layer (at 2 kV) followed by a Ga ion-beam-deposited Pt layer (at 30 kV). Carbon layers were deposited with an electron beam (2 kV) before the Pt coating process. For each Ryugu grain, sections that were a few tens of micrometres in size were extracted using a microsampling manipulator and mounted onto TEM copper grids. After the target samples were attached to the TEM grids, they were thinned to 50 to 200 nm using a 16–30 kV Ga^+ beam and were finally cleaned using a 2 kV Ga^+ beam at 77 pA.

The prepared sections were examined using FE-TEM (JEOL JEM 2100 F) equipped with an EDX (JED-2300T, JEOL) at Kyoto University. Bright-field (BF), dark-field (DF) and high-resolution TEM images as well as selected-area electron-diffraction patterns at 200 kV were obtained using a CCD or CMOS camera (Gatan Orius200D, Rio9). The EDX analysis was performed in STEM mode aided by annular DF imaging. To analyse the spatial variation of the diffraction patterns, 4D-STEM datasets with nanobeam (quasi-parallel beam) illumination were acquired using Gatan Digital Micrograph scripting to control the deflection coils and the CCD camera. Position-averaged nanobeam diffraction (NBD) patterns were extracted from the 4D-STEM datasets. Quantitative elemental abundances were calculated using the ζ -factor method⁴⁹. EDX data were analysed using the JEOL analytical station software. The EDX line profiles were obtained with spatial resolutions of 4.5 nm (magnetite in Extended Data Fig. 1) and 2.8 nm (breunnerite in Extended Data Fig. 5). To improve the signal-to-noise ratio, the line profiles were smoothed by adjacent averaging methods (average of ten neighbouring data points) using the Origin software. Elemental concentration maps were obtained by applying the ζ -factor method for each pixel.

Electron energy-loss spectroscopy analysis

To observe the impact craters on the phyllosilicate, high-resolution TEM imaging, high-angle annular dark-field (HAADF) STEM imaging, EDX and electron energy-loss spectroscopy (EELS) were performed with a monochromated microscope (JEM-ARM200F, JEOL) at the Institute for Chemical Research, Kyoto University. This microscope has a monochromator, an aberration corrector for STEM (CEOS), an EDX system (JED-2300T silicon drift detector 100 GV) and an image filter (Gatan966 Quantum ERS) for EELS. We used a voltage of 200 kV to accelerate the electrons. The probe current was approximately 10 pA for the TEM and STEMs observation and for the EDX and EELS analyses. The typical energy resolution of this EELS analysis was 0.2–0.3 eV, which was determined from the full-width at half-maximum of the measured zero-loss peak. The energy dispersion was 0.25 eV per channel for the analysis of the Fe $L_{2,3}$ edge (Fig. 3) and O K-edge region (Extended Data Fig. 7). The Fourier-ratio deconvolution technique was applied to the O K-edge spectra to remove the effects of plural scattering in the specimen. The difference spectrum in Extended Data Fig. 7 (subtraction) was obtained by subtracting the spectrum of amorphous silicate from the spectrum of the vesicle after scaling the peak intensity of the spectrum of amorphous silicate (multiplication by 0.8).

Calculation of the nitrogen accumulated from the solar wind on the modified magnetite

The duration of space exposure was estimated by assuming that the accumulation of solar wind nitrogen atoms is comparable to the amount of nitrogen in the iron nitride on the modified magnetite. The thickness of iron nitride (T_N) is assumed to be 50 nm (in Fig. 2). The solar wind nitrogen flux (F_N) of 6.02×10^{11} ($\text{cm}^{-2} \text{yr}^{-1}$) was calculated using the flux of solar wind hydrogen ($2.80 \times 10^8 \text{ cm}^{-2} \text{ s}^{-1}$) and the ratio of nitrogen to hydrogen (6.81×10^{-5}) detected at 1 AU by NASA's Genesis mission⁵⁰. Assuming that one nitrogen atom is included in a Fe_4N cubic lattice with a volume of $5.4 \times 10^{-2} \text{ nm}^3$, the number of nitrogen atoms in a Fe_4N slab of $50 \text{ nm} \times 1 \text{ cm} \times 1 \text{ cm}$ is 9.2×10^{16} atoms. The space-exposure duration (D_N) at 1.19 AU (the current average heliocentric distance of Ryugu) is calculated as follows: $D_N = 9.2 \times 10^{16} / F_N \times 1.19^2$. From this estimation, we obtained $D_N = 2.2 \times 10^5 \text{ yr}$.

Evaluation of nitridation of iron metal by ammonia gas in equilibrated vapour with a CI composition

We investigated the nitridation of iron metal by exposure to impact vapour produced on the surface of Ryugu. Molecular N_2 and NH_3 are dominant nitrogen compounds in the equilibrated vapour with a CI chondritic composition^{32,33}. In the stable temperature range of Fe_4N (450–950 K; ref. 51), N_2 is the major N-bearing gas in the CI vapour. The amount of NH_3 is two orders of magnitude lower than that of N_2 (ref. 32). However, molecular N_2 is poorly dissociated for nitridation due to the strong triple bond, and the nitridation requires ultra-high pressures of several tens of gigapascals⁵². Conversely, ammonia gas can be dissociated with metal catalysis, causing absorption and diffusion of nitrogen atoms in the metal³⁴. Experimental data have shown that Fe_4N of 10 nm thickness can be formed on iron metal by 10^{-4} s exposure to $\text{NH}_3\text{-H}_2$ gas of atmospheric pressure at 843 K (ref. 53), although the nitriding rate will be slower at lower temperatures. Therefore, we evaluated the stability field of iron nitride coexisting with ammonia gas in the impact vapour. We calculated the Fe–N–O potential diagram with plots of equilibrated vapour with a CI composition. The temperature range covers the stability field of Fe_4N in the Fe–N phase diagram⁵¹. The Fe–N–O potential diagram, controlled by the nitriding potential ($P[\text{NH}_3]/P[\text{H}_2^{2/2}]$), is calculated using the Gibbs energy of iron metal, magnetite and wüstite from the NIST-JANAF Thermochemical Tables and Fe_4N from Göhring et al.⁵¹. The gas compositions of the equilibrated vapour were calculated by Kuwahara and Sugita³². We adopted the impact conditions with an entropy gain of $3.5 \text{ kJ K}^{-1} \text{ kg}^{-1}$, which corresponds to an impact velocity of

approximately 13 km s^{-1} (ref. 32). The gas composition at 1,000 K was calculated by Schaefer and Fegley³³.

Helium ion irradiation experiment of Ryugu grains

Helium ion irradiation experiments of Ryugu grains were performed to investigate the modification caused by solar wind irradiation. Detailed experimental and analytical procedures are described in Noguchi et al.¹⁰. The ion irradiation experiment was conducted using the ion irradiation system developed at the Institute of Space and Astronautical Science, JAXA. The surface-modified magnetite we investigated (Extended Data Fig. 8) was irradiated by 4 keV helium ions with an ion flux of $\sim 1.5 \times 10^{13}$ ions $\text{cm}^{-2} \text{ s}^{-1}$ and a total dose of helium ions of 1.3×10^{18} ions cm^{-2} .

Data availability

All the data needed to evaluate the conclusions in the paper are presented in the paper or the supplementary information. They will be also available through the JAXA Data Archives and Transmission System (DARTS). (https://data.darts.isas.jaxa.jp/pub/hayabusa2/paper/sample/Matsumoto_2023/). Source data are provided with this paper.

References

- Füri, E. & Marty, B. Nitrogen isotope variations in the Solar System. *Nat. Geosci.* **8**, 515–522 (2015).
- Poch, O. et al. Ammonium salts are a reservoir of nitrogen on a cometary nucleus and possibly on some asteroids. *Science* **367**, eaaw7462 (2020).
- De Sanctis, M. C. et al. Ammoniated phyllosilicates with a likely outer Solar System origin on (1) Ceres. *Nature* **528**, 241–244 (2015).
- Hashizume, K., Marty, B. & Wieler, R. Analyses of nitrogen and argon in single lunar grains: towards a quantification of the asteroidal contribution to planetary surfaces. *Earth Planet. Sci. Lett.* **202**, 201–216 (2002).
- Watanabe, S. et al. Hayabusa2 arrives at the carbonaceous asteroid 162173 Ryugu—A spinning top-shaped rubble pile. *Science* **364**, 268–272 (2019).
- Tachibana, S. et al. Pebbles and sand on asteroid (162173) Ryugu: in situ observation and particles returned to Earth. *Science* **375**, 1011–1016 (2022).
- Yokoyama, T. et al. Samples returned from the asteroid Ryugu are similar to Ivuna-type carbonaceous meteorites. *Science* **379**, eabn7850 (2022).
- Nakamura, T. et al. Formation and evolution of carbonaceous asteroid Ryugu: direct evidence from returned samples. *Science* **379**, eabn8671 (2022).
- Ito, M. A pristine record of outer Solar System materials from asteroid Ryugu's returned sample. *Nat. Astron.* **6**, 1163–1171 (2022).
- Noguchi, T. et al. A dehydrated space-weathered skin cloaking the hydrated interior of Ryugu. *Nat. Astron.* **7**, 170–181 (2023).
- Keller, L. P. & McKay, D. S. Discovery of vapor deposits in the lunar regolith. *Science* **261**, 1305–1307 (1993).
- Sasaki, S., Nakamura, K., Hamabe, Y., Kurahashi, E. & Hiroi, T. Production of iron nanoparticles by laser irradiation in a simulation of lunar-like space weathering. *Nature* **410**, 555–557 (2001).
- Noguchi, T. et al. Incipient space weathering observed on the surface of Itokawa dust particles. *Science* **333**, 1121–1125 (2011).
- Dobrică, E. Nonequilibrium spherulitic magnetite in the Ryugu samples. *Geochim Cosmochim. Acta* **346**, 65–75 (2023).
- Nielsen, H. P. & Buchwald, V. F. Roaldite, a new nitride in iron meteorites. *Lunar Planet. Sci. Conf. Proc.* **12**, 1343–1348 (1982).
- Tan, H., Verbeeck, J., Abakumov, A. & Van Tendeloo, G. Oxidation state and chemical shift investigation in transition metal oxides by EELS. *Ultramicroscopy* **116**, 24–33 (2012).

17. Seto, Y. & Ohtsuka, M. ReciPro: free and open-source multipurpose crystallographic software integrating a crystal model database and viewer, diffraction and microscopy simulators, and diffraction data analysis tools. *J. Appl. Crystallogr.* **55**, 397–410 (2022).
18. Liu, Z. Q., Hashimoto, H., Song, M., Mitsuishi, K. & Furuya, K. Phase transformation from Fe₄N to Fe₃O₄ due to electron irradiation in the transmission electron microscope. *Acta Mater.* **52**, 1669–1674 (2004).
19. Ito, K. et al. Growth and magnetic properties of epitaxial Fe₄N films on insulators possessing lattice spacing close to Si (001) plane. *J. Cryst. Growth* **455**, 66–70 (2016).
20. Frati, F., Hunault, M. O. J. Y. & De Groot, F. M. F. Oxygen K-edge X-ray absorption spectra. *Chem. Rev.* **120**, 4056–4110 (2020).
21. Matsumoto, T., Harries, D., Langenhorst, F., Miyake, A. & Noguchi, T. Iron whiskers on asteroid Itokawa indicate sulfide destruction by space weathering. *Nat. Commun.* **11**, 1117 (2020).
22. Matsumoto, T. et al. Space weathering of iron sulfides in the lunar surface environment. *Geochim. Cosmochim. Acta* **299**, 69–84 (2021).
23. Ziegler, J. F., Ziegler, M. D. & Biersack, J. P. SRIM—the stopping and range of ions in matter. *Nucl. Instrum. Methods Phys. Res. Sect. B Beam Interact. Mater. Atoms* **268**, 1818–1823 (2010).
24. Chaves, L. C. et al. Understanding the effects of space weathering on magnetite through experimental simulations. *LPI Contrib.* **2678**, 2213 (2022).
25. Harries, D. Interface processes and anomalous oxygen transport in rapid metal oxidation and magnetite formation at protoplanetary conditions. *ACS Earth Sp. Chem.* **3**, 2207–2224 (2019).
26. Herbert, F. W., Aravind, K., Lucy, R., Van Vliet, J. K. & Bilge, T. Magnetic diffusion anomaly at the Néel temperature of pyrrhotite, Fe_{1-x}S. *Phys. Chem. Chem. Phys.* **17**, 11036–11041 (2015).
27. Lux, S., Baldauf-Sommerbauer, G. & Siebenhofer, M. Hydrogenation of inorganic metal carbonates: a review on its potential for carbon dioxide utilization and emission reduction. *ChemSusChem* **11**, 3357–3375 (2018).
28. Harries, D., Barth, M. I. F. & Langenhorst, F. Iron nitride in metal of the primitive chondrite Acfer 094: extreme nebular nitrogen processing?. *LPI Contrib.* **2067**, 6079 (2018).
29. Okazaki, R. et al. Noble gases and nitrogen in samples of asteroid Ryugu record its volatile sources and recent surface evolution. *Science* **379**, eabo0431 (2022).
30. Yabuta, H. et al. Macromolecular organic matter in samples of the asteroid (162173) Ryugu. *Science* **379**, eabn9057 (2023).
31. Lodders, K. Relative atomic Solar System abundances, mass fractions, and atomic masses of the elements and their isotopes, composition of the solar photosphere, and compositions of the major chondritic meteorite groups. *Space Sci. Rev.* **217**, 44 (2021).
32. Kuwahara, H. & Sugita, S. The molecular composition of impact-generated atmospheres on terrestrial planets during the post-accretion stage. *Icarus* **257**, 290–301 (2015).
33. Schaefer, L. & Fegley, B. Jr. Chemistry of atmospheres formed during accretion of the Earth and other terrestrial planets. *Icarus* **208**, 438–448 (2010).
34. Mittemeijer, E. J. & Slycke, J. T. Chemical potentials and activities of nitrogen and carbon imposed by gaseous nitriding and carburising atmospheres. *Surf. Eng.* **12**, 152–162 (1996).
35. Kandemir, T., Schuster, M. E., Senyshyn, A., Behrens, M. & Schlögl, R. The Haber–Bosch process revisited: on the real structure and stability of ‘ammonia iron’ under working conditions. *Angew. Chem. Int. Ed.* **52**, 12723–12726 (2013).
36. Somers, M. A. J. Development of the compound layer during nitriding and nitrocarburising of iron and iron-carbon alloys. in *Thermochemical Surface Engineering of Steels* pp. 341–372 (Elsevier, 2015).
37. Pilorget, C. First compositional analysis of Ryugu samples by the MicrOmega hyperspectral microscope. *Nat. Astron.* **6**, 221–225 (2022).
38. Viennet, J.-C. et al. Interaction between clay minerals and organics in asteroid Ryugu. *Geochem. Perspect. Lett.* **25**, 8–12 (2023).
39. Naraoka, H. et al. Soluble organic molecules in samples of the carbonaceous asteroid (162173) Ryugu. *Science* **379**, eabn9033 (2023).
40. Cody, G. D. et al. Quantitative organic and light-element analysis of comet 81P/Wild 2 particles using C-, N-, and O-μ-XANES. *Meteorit. Planet. Sci.* **43**, 353–365 (2008).
41. Ishii, H. A. et al. Multiple generations of grain aggregation in different environments preceded Solar System body formation. *Proc. Natl Acad. Sci.* **115**, 6608–6613 (2018).
42. Yabuta, H. et al. Formation of an ultracarbonaceous Antarctic micrometeorite through minimal aqueous alteration in a small porous icy body. *Geochim. Cosmochim. Acta* **214**, 172–190 (2017).
43. Pizzarello, S., Williams, L. B., Lehman, J., Holland, G. P. & Yarger, J. L. Abundant ammonia in primitive asteroids and the case for a possible exobiology. *Proc. Natl Acad. Sci.* **108**, 4303–4306 (2011).
44. Keller, L. P. & Flynn, G. J. Evidence for a significant Kuiper belt dust contribution to the zodiacal cloud. *Nat. Astron.* **6**, 731–735 (2022).
45. Flynn, G. J. Atmospheric entry heating: a criterion to distinguish between asteroidal and cometary sources of interplanetary dust. *Icarus* **77**, 287–310 (1989).
46. Matrajt, G., Taylor, S., Flynn, G., Brownlee, D. & Joswiak, D. A nuclear microprobe study of the distribution and concentration of carbon and nitrogen in Murchison and Tagish Lake meteorites, Antarctic micrometeorites, and IDPs: implications for astrobiology. *Meteorit. Planet. Sci.* **38**, 1585–1600 (2003).
47. Broadley, M. W., Bekaert, D. V., Piani, L., Füre, E. & Marty, B. Origin of life-forming volatile elements in the inner Solar System. *Nature* **611**, 245–255 (2022).
48. Dzedzic, P., Bartoszewicz, A. & Córdova, A. Inorganic ammonium salts as catalysts for direct aldol reactions in the presence of water. *Tetrahedron Lett.* **50**, 7242–7245 (2009).
49. Watanabe, M. & Williams, D. B. The quantitative analysis of thin specimens: a review of progress from the Cliff-Lorimer to the new ζ-factor methods. *J. Microsc.* **221**, 89–109 (2006).
50. Reisenfeld, D. B. et al. Solar wind conditions and composition during the Genesis mission as measured by in situ spacecraft. *Space Sci. Rev.* **175**, 125–164 (2013).
51. Göhring, H., Fabrichnaya, O., Leineweber, A. & Mittemeijer, E. J. Thermodynamics of the Fe-N and Fe-NC systems: the Fe-N and Fe-NC phase diagrams revisited. *Metall. Mater. Trans. A* **47**, 6173–6186 (2016).
52. Ertl, G., Huber, M. & Thiele, N. Formation and decomposition of nitrides on iron surfaces. *Z. für Naturforsch. A* **34**, 30–39 (1979).
53. Belmonte, T., Gouné, M. & Michel, H. Numerical modeling of interstitial diffusion in binary systems. Application to iron nitriding. *Mater. Sci. Eng. A* **302**, 246–257 (2001).

Acknowledgements

We thank all the members of the Hayabusa2 project for their technical and scientific contributions. This work was funded by the Japan Society for the Promotion of Science (KAKENHI Grant Nos. 21K113981, 21H05431, 19H0094, 19KK0094, 21H05424, 20H00198, 20H00205 and 20K14537).

Author contributions

T. Matsumoto, T. Noguchi, A. Miyake, Y.I. and M.H. performed the SEM and STEM analyses. Y.S., M. Miyahara, N.T., H.S., S.H., D.H., T. Nakamura, M. Matsumoto, H.A.I., J.P.B., K.O., E.D., H.L., C.L.G., D.J., F.d.l.P., S.L., M. Marinova, F.L., P.B., T.H.V.P., R.R., N.M.A., J.G., T.Z., P.-M.Z., M.S.T., R.S., K.B., B.A.C., J.C.B., L.H., M.R.L., L.D., P.A.B., M.E.Z., D.R.F., J. Martinez, A. Tsuchiyama, M. Yasutake, J. Matsuno, S.O., I.M., K.U., M.U., A. Takeuchi,

M.S., S.E. and T. Michikami engaged in the search for space-weathered Ryugu grains. A. Takigawa, Y.N., S. Tachibana, T. Matsumoto and T. Noguchi performed the helium ion irradiation experiments. T. Matsumoto wrote the first draft. T. Matsumoto, T. Noguchi, A. Miyake, Y.I., M.H., D.H., S. Tachibana, N.T., A. Takigawa, M. Miyahara, T. Nakamura, H.A.I., J.P.B., E.D., H.L., P.B., K.B. and J.C.B. discussed the results and commented on the manuscript. K.S., A.N., K.Y., A. Miyazaki, M.N., T.Y., T.O., M.A. and T.U. led the JAXA curation activities for initial characterization of allocated Ryugu particles. H. Yurimoto, T. Nakamura, T. Noguchi, H. Yabuta, R.O., H.N. and S. Tachibana acted as the principal investigators. M. Yoshikawa, T.S., S. Tanaka, F.T., S.N., S.W. and Y.T. administered the Hayabusa2 project.

Competing interests

The authors declare no competing interests.

Additional information

Extended data Extended data are available for this paper at <https://doi.org/10.1038/s41550-023-02137-z>.

Supplementary information The online version contains supplementary material available at <https://doi.org/10.1038/s41550-023-02137-z>.

Correspondence and requests for materials should be addressed to Toru Matsumoto.

Peer review information *Nature Astronomy* thanks the anonymous reviewers for their contribution to the peer review of this work.

Reprints and permissions information is available at www.nature.com/reprints.

Publisher's note Springer Nature remains neutral with regard to jurisdictional claims in published maps and institutional affiliations.

Open Access This article is licensed under a Creative Commons Attribution 4.0 International License, which permits use, sharing, adaptation, distribution and reproduction in any medium or format, as long as you give appropriate credit to the original author(s) and the source, provide a link to the Creative Commons license, and indicate if changes were made. The images or other third party material in this article are included in the article's Creative Commons license, unless indicated otherwise in a credit line to the material. If material is not included in the article's Creative Commons license and your intended use is not permitted by statutory regulation or exceeds the permitted use, you will need to obtain permission directly from the copyright holder. To view a copy of this license, visit <http://creativecommons.org/licenses/by/4.0/>.

© The Author(s) 2023

Toru Matsumoto ^{1,2}✉, **Takaaki Noguchi** ², **Akira Miyake**², **Yohei Igami** ², **Mitsutaka Haruta**³, **Yusuke Seto**⁴, **Masaaki Miyahara** ⁵, **Naotaka Tomioka** ⁶, **Hikaru Saito**^{7,8}, **Satoshi Hata**^{9,10}, **Dennis Harries** ¹¹, **Aki Takigawa** ¹², **Yusuke Nakauchi**¹³, **Shogo Tachibana** ¹⁴, **Tomoki Nakamura**¹⁵, **Megumi Matsumoto**¹⁵, **Hope A. Ishii** ¹⁶, **John P. Bradley**¹⁶, **Kenta Ohtaki**¹⁶, **Elena Dobrică** ¹⁶, **Hugues Leroux**¹⁷, **Corentin Le Guillou**¹⁷, **Damien Jacob** ¹⁷, **Francisco de la Peña**¹⁷, **Sylvain Laforet** ¹⁷, **Maya Marinova**¹⁸, **Falko Langenhorst** ¹⁹, **Pierre Beck**²⁰, **Thi H. V. Phan**²⁰, **Rolando Rebois** ²⁰, **Neyda M. Abreu**²¹, **Jennifer Gray**²², **Thomas Zega** ²³, **Pierre-M. Zanetta**²³, **Michelle S. Thompson**²⁴, **Rhonda Stroud** ²⁵, **Kate Burgess** ²⁶, **Brittany A. Cymes** ^{26,27}, **John C. Bridges**²⁸, **Leon Hicks** ²⁸, **Martin R. Lee**²⁹, **Luke Daly** ^{29,30,31}, **Phil A. Bland**³², **Michael E. Zolensky** ³³, **David R. Frank**¹⁶, **James Martinez**³⁴, **Akira Tsuchiyama** ^{35,36,37}, **Masahiro Yasutake**³⁸, **Junya Matsuno**³⁶, **Shota Okumura** ², **Itaru Mitsukawa**², **Kentaro Uesugi** ³⁸, **Masayuki Uesugi** ³⁸, **Akihisa Takeuchi** ³⁸, **Mingqi Sun** ^{36,37,39}, **Satomi Enju**⁴⁰, **Tatsuhiko Michikami** ⁴¹, **Hisayoshi Yurimoto** ⁴², **Ryuji Okazaki**⁴³, **Hikaru Yabuta** ⁵, **Hiroshi Naraoka**⁴³, **Kanako Sakamoto** ¹³, **Toru Yada** ¹³, **Masahiro Nishimura**¹³, **Aiko Nakato**¹³, **Akiko Miyazaki** ⁴⁴, **Kasumi Yogata** ¹³, **Masanao Abe**^{13,45}, **Tatsuaki Okada** ^{13,45}, **Tomohiro Usui** ^{13,45}, **Makoto Yoshikawa**^{13,45}, **Takanao Saiki**^{13,45}, **Satoshi Tanaka**^{13,45}, **Fuyuto Terui**⁴⁶, **Satoru Nakazawa** ^{13,45}, **Sei-ichiro Watanabe** ⁴⁷ & **Yuichi Tsuda**^{13,45}

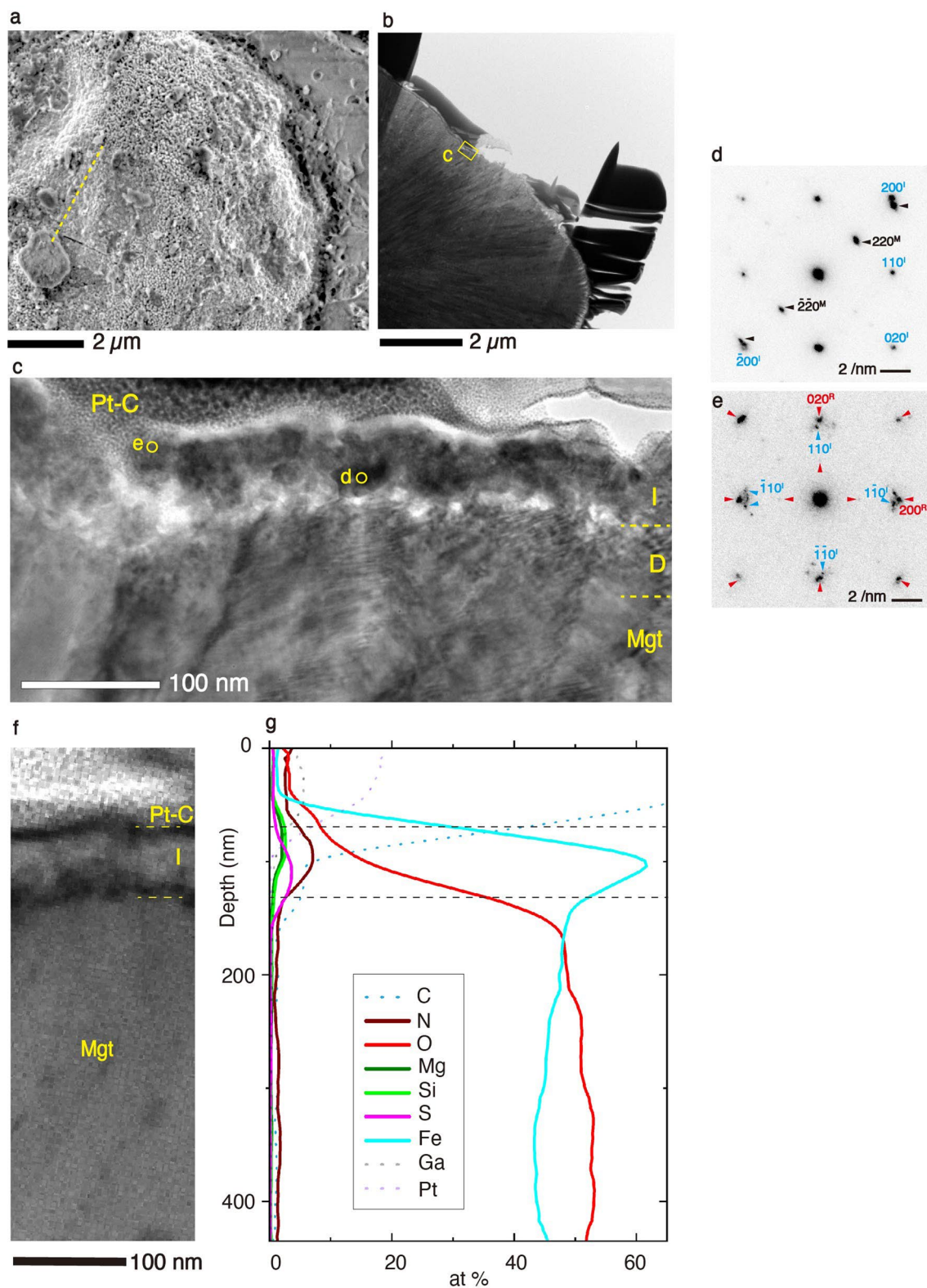
¹The Hakubi Center for Advanced Research, Kyoto University, Kyoto, Japan. ²Division of Earth and Planetary Sciences, Kyoto University, Kyoto, Japan.

³Institute for Chemical Research, Kyoto University, Uji, Japan. ⁴Department of Geosciences, Osaka Metropolitan University, Osaka, Japan. ⁵Earth and Planetary Systems Science Program, Hiroshima University, Higashi-Hiroshima, Japan. ⁶Kochi Institute for Core Sample Research, X-Star, JAMSTEC, Nankoku, Japan. ⁷Institute for Materials Chemistry and Engineering, Kyushu University, Fukuoka, Japan. ⁸Pan-Omics Data-Driven Research Innovation Center, Kyushu University, Fukuoka, Japan. ⁹Department of Advanced Materials Science, Kyushu University, Fukuoka, Japan. ¹⁰The Ultramicroscopy Research Center, Kyushu University, Fukuoka, Japan. ¹¹Luxembourg Institute of Science and Technology, European Space Resources Innovation Centre, Belvaux, Luxembourg. ¹²Department of Earth and Planetary Science, University of Tokyo, Tokyo, Japan. ¹³Institute of Space and Astronautical Science, Japan Aerospace Exploration Agency, Sagami, Japan. ¹⁴UTokyo Organization for Planetary and Space Science, University of Tokyo, Tokyo, Japan.

¹⁵Department of Earth Science, Graduate School of Science, Tohoku University, Sendai, Japan. ¹⁶Hawai'i Institute of Geophysics & Planetology, the University of Hawai'i at Mānoa, Honolulu, HI, USA. ¹⁷Université de Lille, CNRS, INRAE; Centrale Lille, UMR 8207-UMET-Unité Matériaux et Transformations, Lille, France. ¹⁸Université de Lille, CNRS, INRAE; Centrale Lille, Université Artois, FR 2638-IMEC-Institut Michel-Eugène Chevreul, Lille, France. ¹⁹Institute of Geoscience, Friedrich Schiller University Jena, Jena, Germany. ²⁰Institut de Planétologie et d'Astrophysique de Grenoble (IPAG), Université Grenoble Alpes, Grenoble, France. ²¹Langley Research Center, NASA, Hampton, VA, USA. ²²Materials Characterization Lab, The Pennsylvania State University, University Park, PA, USA. ²³Lunar and Planetary Laboratory, Department of Planetary Sciences, University of Arizona, Tucson, AZ, USA. ²⁴Department of Earth, Atmospheric and Planetary Sciences, Purdue University, West Lafayette, IN, USA. ²⁵Buseck Center for Meteorite Studies, Arizona State University, Tempe, AZ, USA. ²⁶U.S. Naval Research Laboratory, Washington, DC, USA. ²⁷Jacobs, NASA Johnson Space Center, Houston, TX, USA. ²⁸Space Research Centre, University of Leicester, Leicester, UK. ²⁹School of Geographical and Earth Sciences, University of Glasgow, Glasgow, UK. ³⁰Australian Centre for Microscopy and Microanalysis, University of Sydney, Sydney, New South Wales, Australia. ³¹Department of Materials, University of Oxford, Oxford, UK.

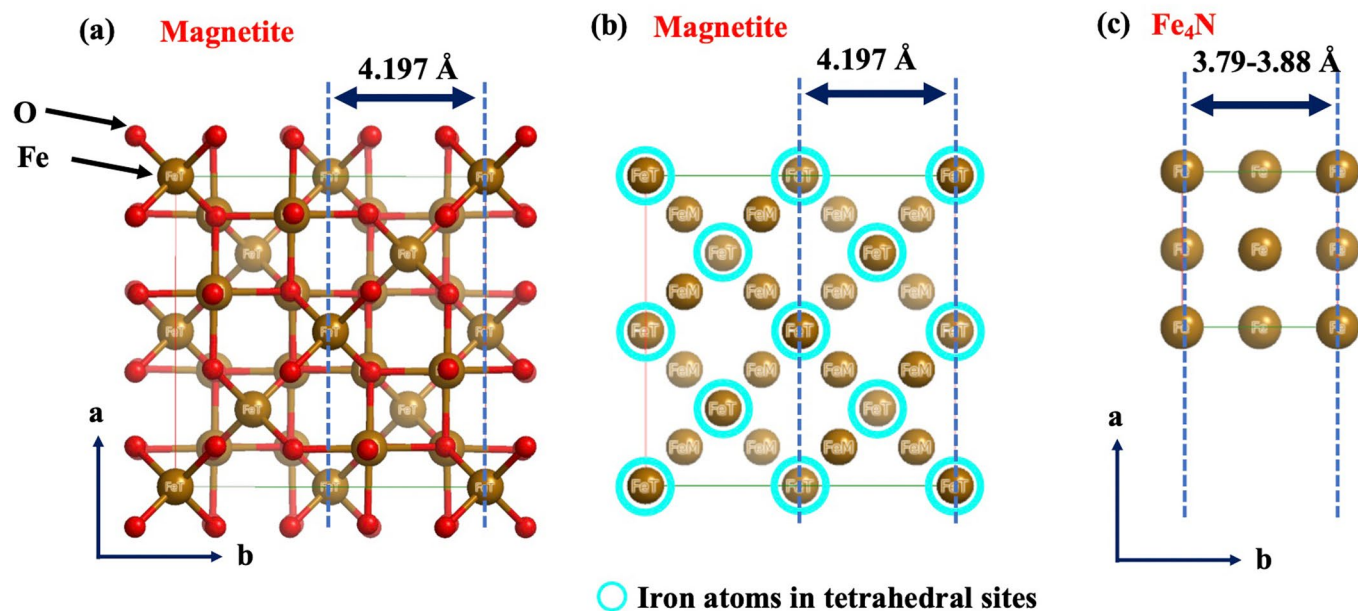
³²School of Earth and Planetary Sciences, Curtin University, Perth, Western Australia, Australia. ³³ARES, NASA, Johnson Space Center, Houston, TX, USA.

³⁴Jacobs Engineering, Dallas, TX, USA. ³⁵Research Organization of Science and Technology, Ritsumeikan University, Kusatsu, Japan. ³⁶CAS Key Laboratory of Mineralogy and Metallogeny/Guangdong Provincial Key Laboratory of Mineral Physics and Materials, Guangzhou Institute of Geochemistry, Chinese Academy of Sciences (CAS), Guangzhou, China. ³⁷CAS Center for Excellence in Deep Earth Science, Guangzhou, China. ³⁸Japan Synchrotron Radiation Research Institute, Sayō, Japan. ³⁹University of Chinese Academy of Sciences, Beijing, China. ⁴⁰Department of Mathematics, Physics, and Earth Science, Ehime University, Matsuyama, Japan. ⁴¹Faculty of Engineering, Kindai University, Higashi-Hiroshima, Japan. ⁴²Department of Earth and Planetary Sciences, Hokkaido University, Sapporo, Japan. ⁴³Department of Earth and Planetary Sciences, Kyushu University, Fukuoka, Japan. ⁴⁴Marine Works Japan Ltd., Yokosuka, Japan. ⁴⁵The Graduate University for Advanced Studies, SOKENDAI, Hayama, Japan. ⁴⁶Department of Mechanical Engineering, Kanagawa Institute of Technology, Atsugi, Japan. ⁴⁷Department of Earth and Environmental Sciences, Nagoya University, Nagoya, Japan.
✉ e-mail: matsumoto.toru.2z@kyoto-u.ac.jp



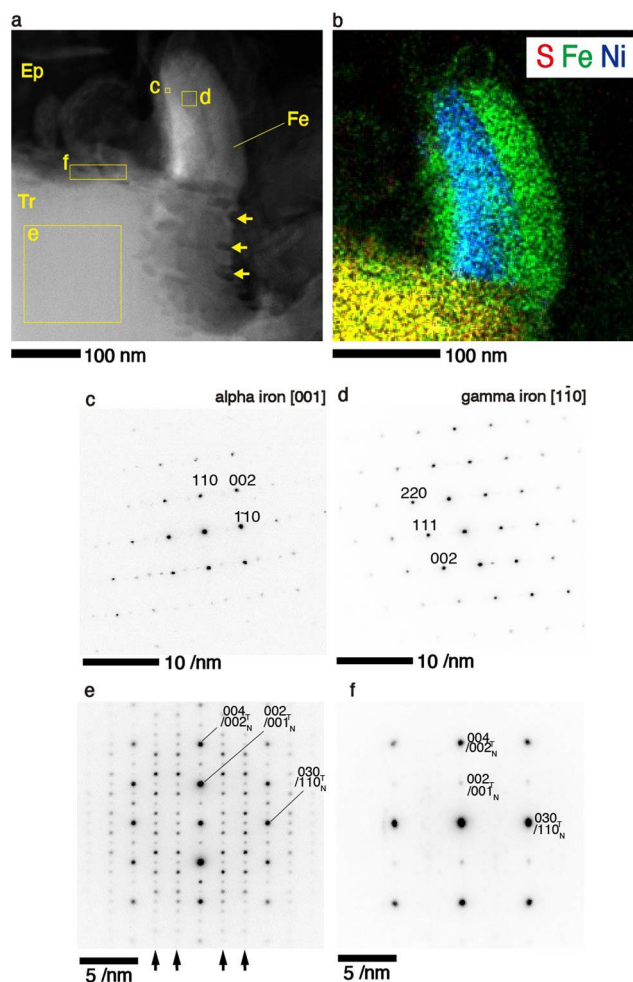
Extended Data Fig. 1 | TEM analysis of modified spherulitic magnetite. **a.** SE image of a spherulitic magnetite embedded in phyllosilicate. The dotted line shows an extraction location for cross sectional TEM analysis. **b.** BF-TEM image of a FIB section extracted from the grain surface in (a). **c.** BF-TEM image of the modified surface of magnetite (Mgt). The magnetite surface is covered by an iron-rich layer (I). The damaged region (D) in magnetite includes crystallographic distortion that shows distinct contrast compared to the substrate. Pt-C is the protective platinum coat. **d, e.** Position-averaged NBD patterns obtained from circled areas in (c), suggestive of magnetite (superscript M), body-centered cubic

(bcc) iron (superscript I), and roaldite (superscript R). Black, blue, and red arrows indicate diffraction spots from magnetite, bcc-iron, and roaldite, respectively. **f.** HAADF-STEM image of the magnetite surface corresponding to the elemental profile in (g). **g.** Depth profile of major elements detected near the magnetite surface. The iron-rich layer is located between the dotted lines. Increase in carbon content at the top surface of the magnetite is due mainly to the carbon protective coat and residual carbon compounds in the platinum protective coat. Sample ID is A0104-026006.



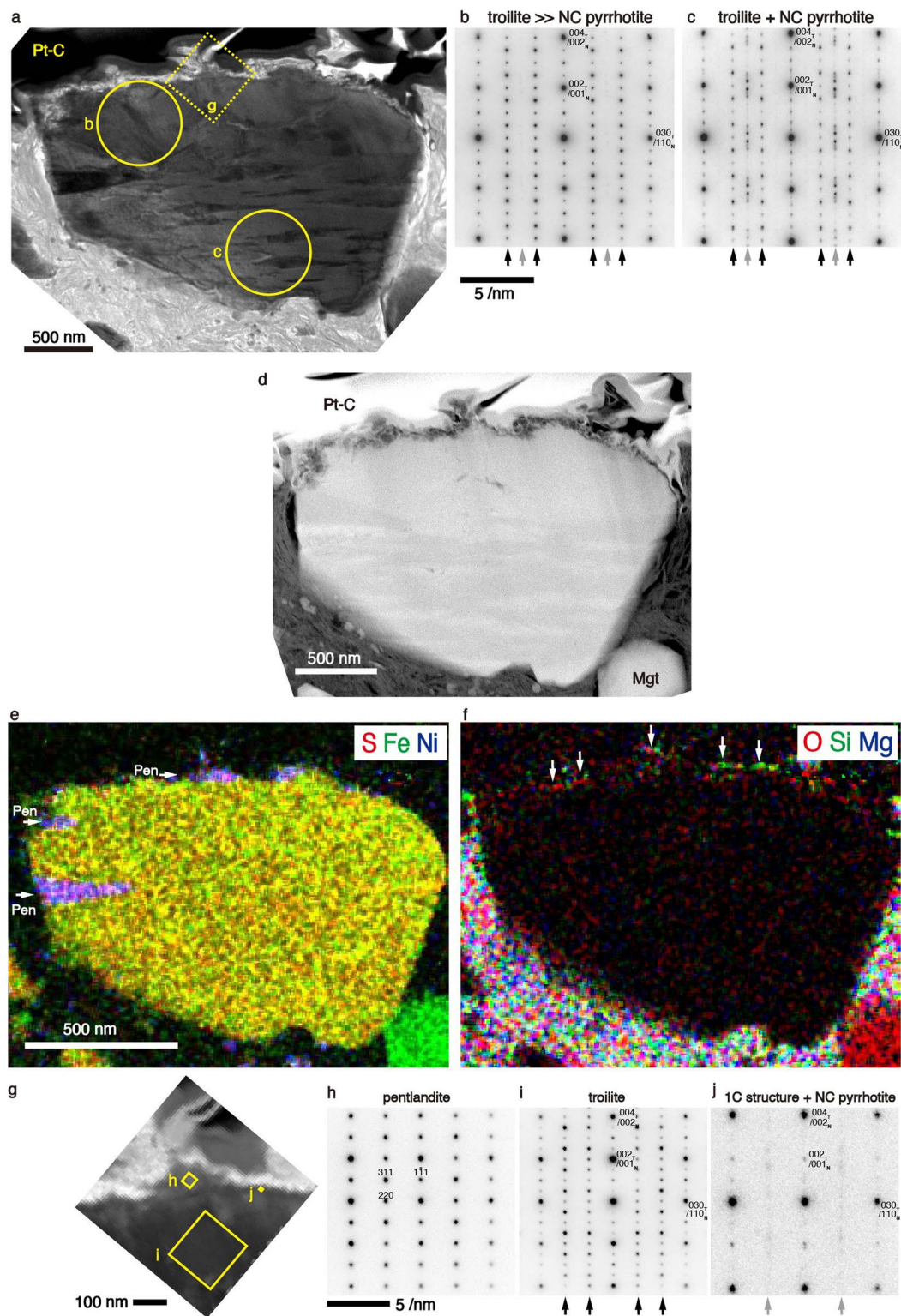
Extended Data Fig. 2 | Atomic arrangement of magnetite and iron nitride (Fe_4N). **a.** Crystal structure of magnetite from the view along the c -axis. Red and brown circles indicate oxygen and iron atoms in magnetite, respectively. **b.** Atomic arrangement of iron in magnetite. Iron atoms in tetrahedral sites are indicated by cyan circles. Distance between the (200) plane (2.099 Å) of

magnetite is shown. **c.** Crystal structure of Fe_4N from the view along the c -axis. Distance between the (100) plane of Fe_4N (1.895–1.94 Å) are measured values from the cubic crystals on space-weathered magnetite in A0104-026006 and A0104-028098. These schematic images were made using the Recipro software (Seto, Y. & Ohtsuka, M, 2022)¹⁷.



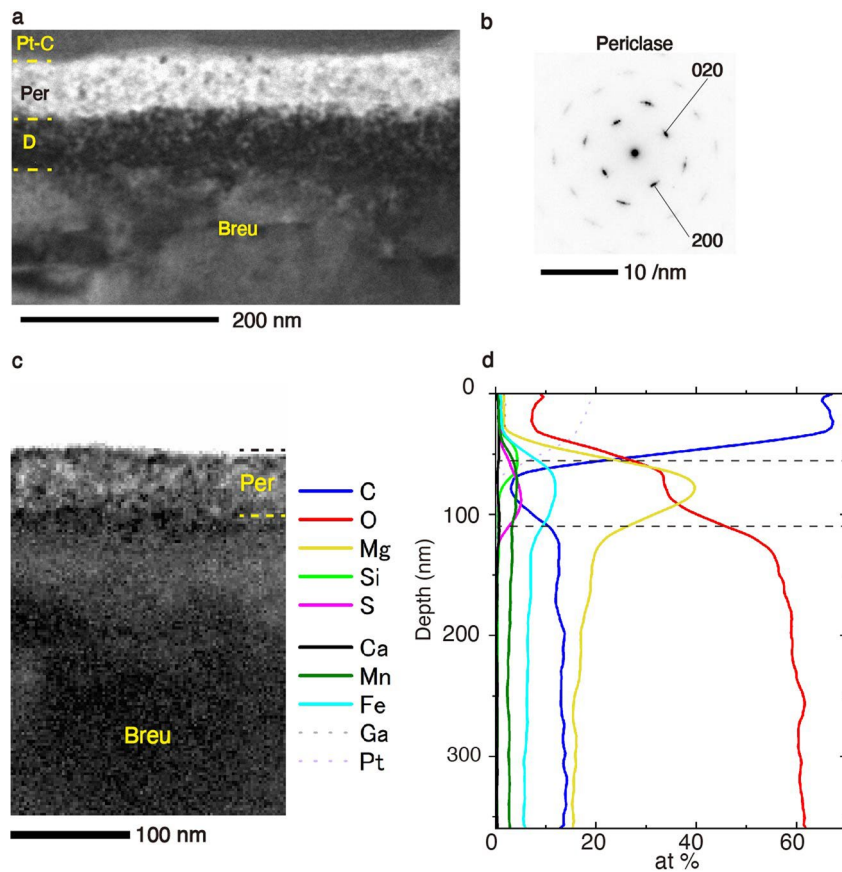
Extended Data Fig. 3 | TEM/STEM analysis of modified iron sulfide in Ryugu grain. **a.** High-Angle Annular-Dark field (HAADF) scanning transmission electron microscope (STEM) image of the modified sulfide. Fe, Tr, and Ep indicate a metallic iron whisker, troilite, and epoxy resin, respectively. Arrows indicate surface open pores on the modified sulfides. **b.** STEM-EDS elemental map of the modified iron sulfide, including sulfur (red), iron (green), and nickel (blue).

c-d. Nanobeam electron diffraction (NBD) pattern of the iron whisker in (a), showing the structure of body-centered-cubic iron (c) and face-centered-cubic iron (d). **e-f.** Position-averaged NBD patterns of iron sulfide obtained from interior (e) and from sulfide surface (f). Both patterns are indexed based on the NiAs-type subcell (superscript N) and troilite (superscript T). Arrows in (e) denote superstructures of troilite. Sample ID is A0104-021002.



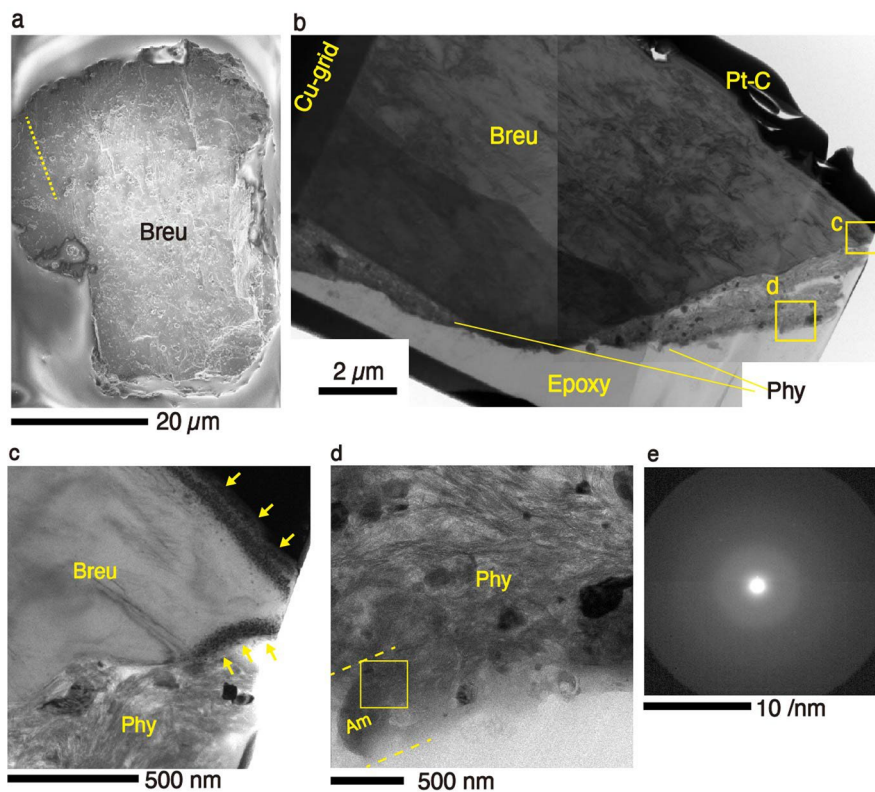
Extended Data Fig. 4 | Modified iron sulfide grain including pentlandite, pyrrhotite (Fe $_{1-x}$ S) and troilite (FeS). **a.** BF-TEM image of the iron sulfide. The grain surface is protected by a platinum coat (Pt-C). **b-c.** Selected area electron diffraction patterns of the iron sulfides obtained from circled areas in **(a)**. Diffraction pattern near the grain surface **(b)** is dominated by troilite, while that from the inner region **(c)** consists of equal amount of troilite and non-integral (NC) pyrrhotite. Both patterns are indexed based on the NiAs-type subcell (superscript N) and troilite (superscript T). Black and gray arrows denote superstructures of troilite and pyrrhotite, respectively. **d.** HAADF-STEM image

of the modified sulfide grain. **e-f.** STEM-EDS elemental maps of the modified iron sulfide. Composite color map in **(e)** consists of sulfur (red), iron (green), and nickel (blue). Arrows in **(e)** show pentlandite lamellae. Composite color map in **(f)** consists of oxygen (red), silicon (green), and magnesium (blue). Arrows in **(f)** show silicon and magnesium-rich layer that is possibly vapor-deposited materials. **g.** BF-STEM image near the surface of the modified sulfide grain shown in **(a)** constructed from a STEM-NBD dataset. **(h-j).** Position averaged NBD patterns of pentlandite at grain surface **(h)** and those obtained from interior of the iron.



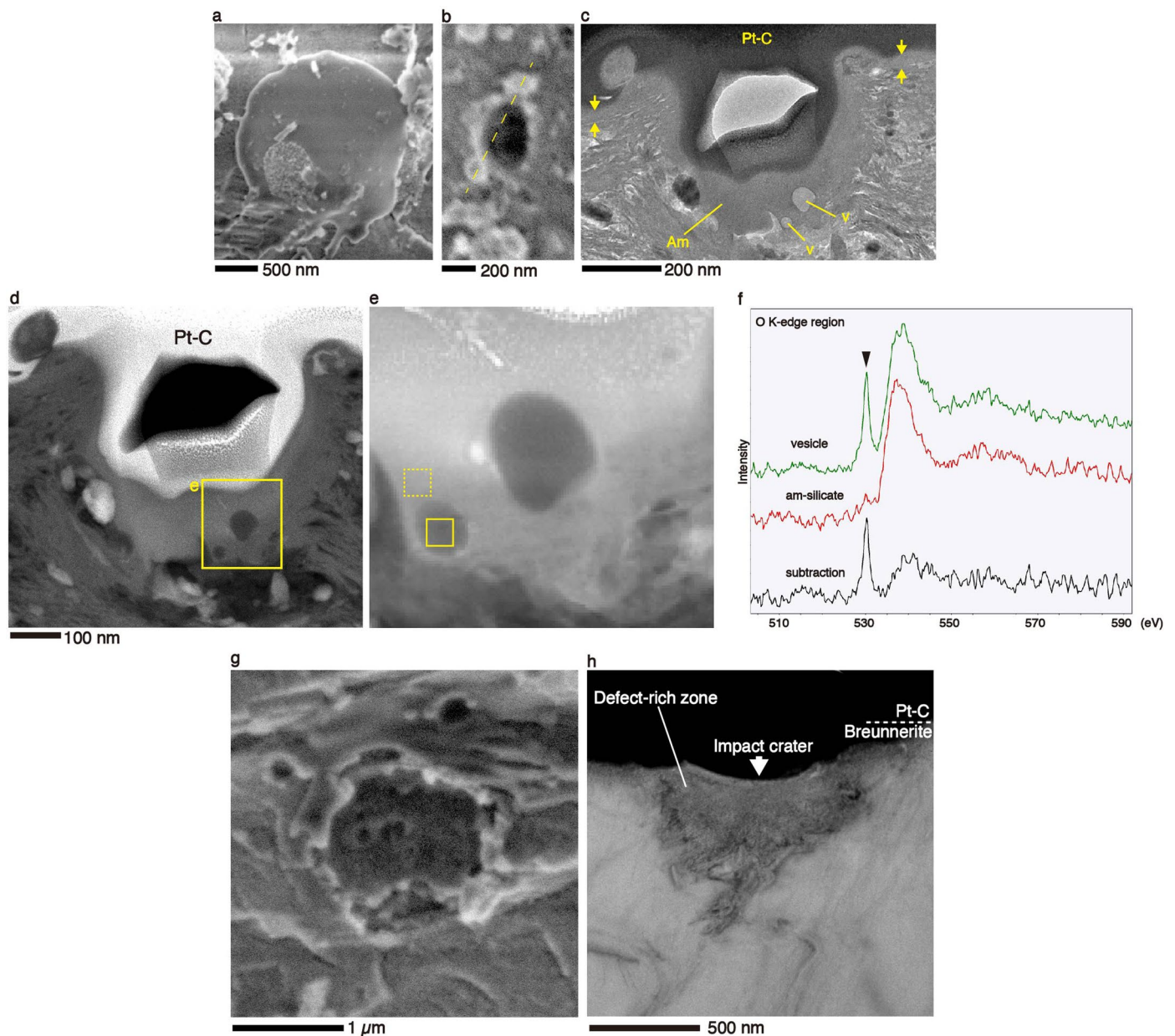
Extended Data Fig. 5 | TEM analysis of modified breunnerite in Ryugu grain. **a.** BF-TEM image of a modified surface of breunnerite (Breu) covered by a ferropericlase-rich layer (Per). The damaged region (D) of the breunnerite includes crystallographic distortion that shows distinct contrast compared to the substrate. **b.** Position averaged NBD pattern of ferropericlase (zone axis of [001]) obtained from the ferropericlase-rich layer. **c.** HAADF-STEM image of

the breunnerite surface (Breu) corresponding to the elemental profile in **(d)**. **d.** Depth profile of major elements detected near the breunnerite surface. The ferropericlase-rich layer (Per) is located between the dotted lines. Increase in carbon content at the top surface of the ferropericlase layer is derived from residual carbon compounds in the protective platinum coat. Sample ID is A0104-021004.



Extended Data Fig. 6 | Modified phyllosilicates coexisting with modified carbonate in Ryugu grain. **a.** SE image of a fine grain of breunnerite (Breu) embedded in epoxy resin. **b.** BF-TEM image of a FIB section extracted from the location indicated by the yellow line in **(a)**. Phyllosilicate (Phy) appears on the opposite side of the breunnerite surface shown in **(a)**. Pt-C, Epoxy, and Cu-grid are protective platinum coat, epoxy resin, and copper FIB grid, respectively.

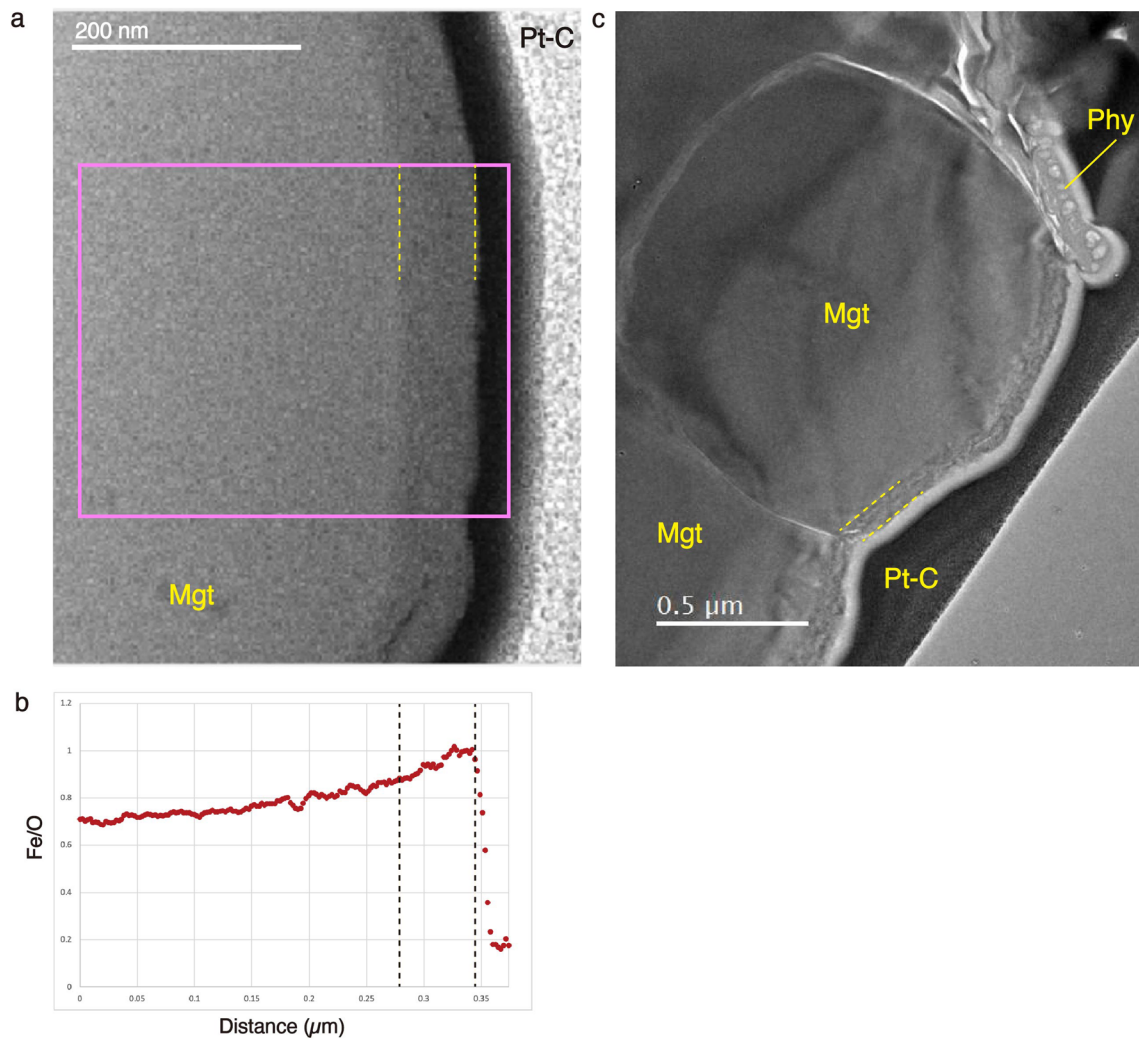
Boxes correspond to the positions of BF-TEM images in **(c, d)**. **c.** BF-TEM image of phyllosilicate surface included in the FIB section. Arrows indicate the modified breunnerite surfaces. **d.** The modified phyllosilicate surface that has an amorphous rim (Am) as indicated by the dotted line. **(e)** Position-averaged NBD pattern of amorphous rim on phyllosilicate obtained from the square area indicated in **(d)**. Sample ID is A0104-021004.



Extended Data Fig. 7 | Melt deposit and impact craters on Ryugu grains.

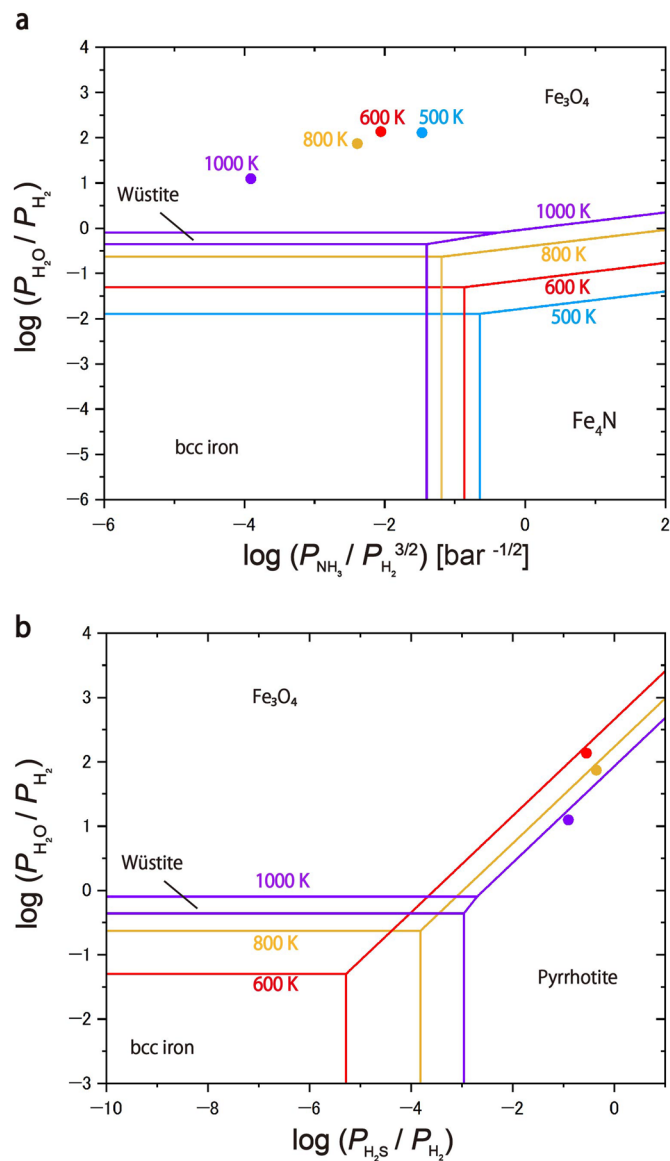
a. SE image of a silicate melt on a carbonate surface. **b.** SE image of an impact crater on phyllosilicate. The dotted line denotes an extraction location of a FIB section for transmission electron microscope (TEM) analysis. **c.** BF-TEM image of the impact crater in (b). The crater floor consists of an amorphous zone (Am) including vesicles (V). The arrows indicate the space-weathered rim of phyllosilicate. The grain surface is protected by a platinum coat (Pt-C). **d.** HAADF-STEM image of the impact crater. The open box corresponds to an enlarged image of the crater floor shown in (e). **e.** HAADF-STEM image of the amorphous region in the crater floor with dimensions of $187\text{ nm} \times 208\text{ nm}$.

Solid-line box and dotted-line box are $15\text{ nm} \times 15\text{ nm}$ in size, and show analysis areas of a vesicle region and an amorphous region, respectively, for electron energy-loss spectra. **f.** Oxygen *K*-edge spectra of the vesicle region (vesicle) and the amorphous region (am-silicate). The black triangle denotes a sharp π^* peak of oxygen at 531 eV. The bottom spectrum (subtraction) is produced by subtracting the spectrum of the vesicle from the amorphous spectrum (see Methods). **g.** SE image of the impact crater on breunnerite surface. **h.** BF-TEM image of the crater on breunnerite. Dark contrast beneath the crater floor corresponds to the defect-rich zone. Pt-C is the protective platinum coat. Sample IDs are A0104-021002 (b-f) and A0104-021004 (a, g, h).



Extended Data Fig. 8 | Magnetite on Ryugu grain (C107-He-01-01) irradiated by 4 keV He⁺ ions with the total dose of 1.3×10^{18} ions/cm². **a.** HAADF-STEM image of the irradiated magnetite (Mgt). The modified surface shows low Z-contrast region possibly due to swelling by helium accumulation (dotted lines in **a** and **b**). The magnetite surface is covered by carbon (dark region) and

platinum deposition (Pt-C) during FIB-processing. **b.** Depth profile of the iron to oxygen ratio in the irradiated magnetite obtained from the box area indicated in (**a**). **c.** BF-TEM image of the irradiated magnetite. Damaged surface regions are indicated by dotted lines. The phyllosilicate surface (Phy) in the periphery of the magnetite shows vesicular structures due to helium accumulation.



Extended Data Fig. 9 | Stability of iron compounds and equilibrated vapors with CI carbonaceous chondrite composition. **a.** Fe-N-O potential diagram and plots of equilibrated vapors with CI composition. Horizontal and vertical axes are the nitriding potential and the ratio of partial pressure of H_2O to H_2 , respectively. **b.** Fe-S-O potential diagram and plots of equilibrated vapors with CI composition. Horizontal and vertical axes are the ratio of partial pressure of H_2S to H_2 , and

that of H_2O to H_2 , respectively. The colored lines show the phase boundaries of iron compounds for various temperatures. Colored circles indicate the gas compositions of equilibrated impact vapors with CI chondrite chemical compositions. Blue, red, yellow, and purple colors denote 500 K, 600 K, 800 K, 1000 K, respectively.